RSC
Applied Interfaces

PAPER

View Article Online
View Journal | View Issue

Check for updates

Cite this: *RSC Appl. Interfaces*, 2024, **1**, 1419

Preparation and characterization of new solid electrolytes $Na_{3-x}Zn_{1-x}Al_{1+x}S_4$†

Tomoya Otono, Hamdi Ben Yahia, Chie Hotehama, Kota Motohashi,
Atsushi Sakuda * and Akitoshi Hayashi *

Received 31st July 2024,
Accepted 10th September 2024

DOI: 10.1039/d4lf00275j

rsc.li/RSCApplInter

Sulfide solid electrolytes, known for their high ionic conductivity and formability, are key materials for the practical use of all-solid-state sodium batteries. In this study, new sulfide solid electrolyte materials, $Na_{3-x}Zn_{1-x}Al_{1+x}S_4$ ($x \le 0.2$), were prepared *via* a self flux synthesis route, using reagents such as Na_2S, Zn, Al, and S. The new materials were characterized using X-ray powder diffraction, Raman spectroscopy, and electrochemical impedance spectroscopy. $Na_{3-x}Zn_{1-x}Al_{1+x}S_4$ formed a solid solution up to $x = 0.2$ and crystallized with a β-$Ca_3Ga_2N_4$-type structure. As the Al content increased, the number of sodium vacancies also increased, resulting in improved ionic conductivity. Among $Na_{3-x}Zn_{1-x}Al_{1+x}S_4$ samples, $Na_{2.9}Zn_{0.9}Al_{1.1}S_4$ exhibited the highest ionic conductivity of 4.5×10^{-6} S cm^{-1} at 25 °C and lowest activation energy of 32 kJ mol^{-1}. Furthermore, the $Na_{2.9}Zn_{0.9}Al_{1.1}S_4$ phase was relatively stable when exposed to humid air, which facilitated its practical use in all-solid-state sodium batteries.

Introduction

Sodium secondary batteries are promising for large-scale energy storage devices owing to the abundance of sodium resources and low cost.[1–3] All-solid-state sodium secondary batteries are expected to meet both safety requirements and low cost.[4] Solid electrolytes are key materials for the practical application of all-solid-state sodium batteries.[5,6] Among these, sulfide solid electrolytes exhibit the highest ionic conductivities and formabilities.[7] We previously reported that Na_3PS_4 glass–ceramics exhibited an ionic conductivity of 2.0×10^{-4} S cm^{-1} and that all-solid-state sodium cells with Na_3PS_4 glass–ceramics operated reversibly at 25 °C for the first time.[8] Various sulfide electrolytes, such as $Na_{11}Sn_2PS_{12}$ and Na_3SbS_4-based electrolytes, have been investigated.[9–17] Particularly, $Na_{2.88}Sb_{0.88}W_{0.12}S_4$ solid electrolytes, where Sb in Na_3SbS_4 was partially replaced by W, exhibited the highest ionic conductivity of 1.25×10^{-1} S cm^{-1} at 25 °C.[17] Sulfide electrolytes generate H_2S gas when exposed to humid air. To increase the stability in humid environments, substitutions of sulfur with oxygen and nitrogen in sulfide electrolytes have been explored.[18,19] Furthermore, electrolytes using a softer acid as a central element were also investigated.[20–22] Among them, Na_3SbS_4-based electrolytes exhibited the highest ionic conductivity and stability under humid environments.[12–16] However, Na_3SbS_4-based electrolytes had low reduction stabilities and narrow electrochemical windows.[23–25] To construct safe all-solid-state sodium batteries, sulfide electrolytes with high ionic conductivity, high tolerance to humidity, and high reduction stability are required.

Recently, Na_3ZnGaS_4-based sulfide electrolytes have been reported.[26–29] Na_3ZnGaS_4 with a framework of corner-shared $(Zn/Ga)_4S_{10}$ super-tetrahedra structure exhibits an ionic conductivity of 3.0×10^{-7} S cm^{-1} at room temperature, and its ionic conductivity can be increased to over 10^{-4} S cm^{-1} by tuning the relative ratio of Zn/Ga and introducing sodium vacancies.[27] When the Na_3ZnGaS_4-based electrolytes were exposed to humid air, H_2S gas was not generated, and X-ray powder diffraction (XRPD) patterns did not change, suggesting that Na_3ZnGaS_4-based electrolytes have high humidity stability.[27–29] Moreover, the Na_2Sn symmetric cell of Na_3ZnGaS_4-based electrolytes operated stably, suggesting that among sulfide solid electrolytes, Na_3ZnGaS_4-based electrolytes have relatively high stability for negative electrodes.[27–29] Among the samples of Na_3ZnMS_4 (M = 13th group elements), the structures of Na_3ZnGaS_4 and Na_3ZnInS_4 have been previously reported;[30] however, the structure of Na_3ZnAlS_4 has not been reported to date. Na_3ZnAlS_4-based electrolytes are expected to exhibit high ionic conductivities, similar to those of Na_3ZnGaS_4-based electrolytes. Moreover, aluminum is the second most abundant resource in the Earth's crust,[3] and Na_3ZnAlS_4-based electrolytes can be synthesized at low costs.

Na_3ZnAlS_4-based electrolytes can be synthesized using sodium polysulfides. Sulfide electrolytes can be synthesized

---

Department of Applied Chemistry, Graduate School of Engineering, Osaka Metropolitan University, 1-1 Gakuen-cho, Naka-ku, Sakai, Osaka 599-8531, Japan. E-mail: saku@omu.ac.jp, akitoshihayashi@omu.ac.jp; Fax: +81 72 2549334; Tel: +81 72 2549331

† Electronic supplementary information (ESI) available. See DOI: **https://doi.org/10.1039/d4lf00275j**

using sodium polysulfides *via* an ambient-pressure heat treatment without a sealing process. Moreover, sodium polysulfides are used as self-fluxes, and aluminum elements can be used as aluminum sources instead of Al_2S_3, which is challenging to obtain as a high-purity starting material.[17]

In this study, we synthesized the new material Na_3ZnAlS_4 with the β-$Ca_3Ga_2N_4$-type structure using sodium polysulfides. $Na_{3-x}Zn_{1-x}Al_{1+x}S_4$ samples, in which sodium vacancies were introduced to increase the ionic conductivity, were also synthesized and their ionic conductivities and moisture stabilities were evaluated.

Experimental section

Synthesis

The $Na_{3-x}Zn_{1-x}Al_{1+x}S_4$ (x = 0, 0.1, 0.15, and 0.2) samples were prepared *via* a simple heat treatment synthesis route using stoichiometric mixtures of Na_2S (99.1%; Nagao), Zn (99.99%; Fujifilm Wako Chem.), Al (99.9%; Kojundo Chem.), and S (99.99%; Kojundo Chem.). The reagents were placed in carbon crucibles and heated in an electric furnace at 750 °C for 17 h under ambient pressure, followed by quenching at room temperature. During synthesis, sodium polysulfide melts were produced and reacted with Zn and Al. $Na_{3-x}Zn_{1-x}Al_{1+x}S_4$ (x = 0, 0.1, 0.15, 0.2) samples did not melt at 750 °C. All processes were performed inside a glove box under a dry Ar atmosphere.

Characterization

The X-ray powder diffraction (XRPD) patterns of the prepared materials were measured with a Rigaku SmartLab diffractometer with a Cu-K_α radiation source, using Bragg–Brentano geometry. X-ray data were collected in a 2θ range of 5.0–120.0° in steps of 0.01°. The data were refined by Le Bail profile analysis using JANA2006 software,[31] and crystal structures were confirmed by Rietveld refinement. In the first step, we performed a Lebail profile fitting analysis. In this step, the cell parameters, the origin shift, the background, and the profile function (pseudo-Voigt) were refined. Once good *R* values were obtained, we fixed all these parameters as the initial cell parameter. In the second step, we analyzed the crystal structure. We included the atomic positions from the isostructural compound Na_3ZnGaS_4, and we refined their coordinates, their thermal parameters and the scale factor. Once the reliability factors converged to low values, we refined all parameters including those of the profile.

The Raman spectra of the samples were measured with a Raman spectrophotometer (LabRAM HR-800; Horiba) using a 532 nm solid-state laser. The samples were placed in a vessel, sealed airtight with a cover glass, and placed in a glovebox under a dry Ar atmosphere.

The morphology and the elements distribution were observed using scanning electron microscope (SEM) (SU8220; Hitachi High Technologies) equipped with an energy dispersive X-ray spectroscopy system (EDS) (EMAX Evolution; Horiba Ltd.).

The ionic conductivities were determined using an impedance analyzer (Solartron; 1260) *via* an alternating current (AC) impedance measurement in the frequency range of 0.1 Hz to 10 MHz, under an applied voltage of 50 mV. Measurements were performed using compressed powder pellets (diameter: 10 mm; thickness: 1 mm). Gold thin films (diameter: 10 mm) were deposited as ion-blocking electrodes on both faces of the pellets using a quick coater (Quick Coater SC-701; Sanyu Electron). Each pellet was sealed in a laminate-type pouch cell to prevent exposure to air.

The humidity stability of the $Na_{2.9}Zn_{0.9}Al_{1.1}S_4$ electrolyte was evaluated by exposing the powder to an air flow at 70% relative humidity for 30 min at room temperature. Subsequently, the powder was analyzed using XRPD and Raman spectroscopy.

Results and discussion

The XRPD pattern of Na_3ZnAlS_4, shown in Fig. 1, is significantly similar to those of Na_3ZnGaS_4 and Na_3ZnInS_4. This suggests that the three phases were isostructural. Consequently, by adjusting the cell parameters of Na_3ZnGaS_4, a full pattern matching was performed successfully. This yielded the refined cell parameters of a = 12.9206(1) Å, c = 18.5822(2) Å, and V = 3102.12(4) Å^3 for Na_3ZnAlS_4. This analysis revealed the presence of impurity peaks at 18.6°, 24.7°, 26.5°, 38.7°, 38.8°, 83.2°, and 83.4°. These peaks were excluded, and Rietveld refinement was performed by using the atomic positions of Na_3ZnGaS_4 as the starting model. Only the Ga atom at the 32*g* Wyckoff position was replaced by Al. With isotropic atomic displacement parameters (ADPs), the reliability factors converged to satisfactory values. However, the Na2 atom displayed a much larger ADP than Na1 (0.087 Å^2 *vs.* 0.035 Å^2). Therefore, anisotropic ADPs were applied to Na2 atoms. This resulted in the final reliability factors, refined atomic positions, and anisotropic ADPs listed in Tables 1–3, respectively. Fig. 2 shows the excellent agreement between the experimental and calculated patterns.

The crystal structure of Na_3ZnAlS_4 is shown in Fig. 3. Na_3ZnAlS_4 crystallizes in a β-$Ca_3Ga_2N_4$-type structure.[32] The structure was composed of $(Zn/Al)S_4$ tetrahedra that shared corners and formed $(Zn/Al)_4S_{10}$ clusters (Fig. 3b). These

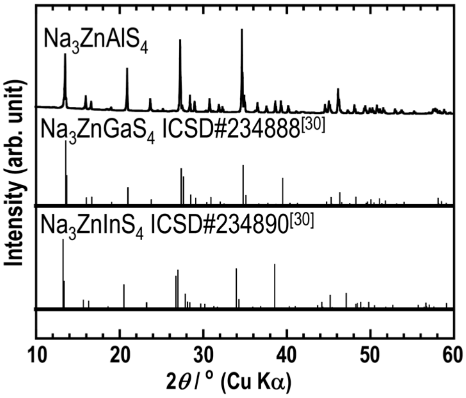

Fig. 1 Experimental XRPD pattern of Na_3ZnAlS_4 and calculated patterns of Na_3ZnInS_4 and Na_3ZnGaS_4.

Table 1 Crystallographic data and structure refinement for Na_3ZnAlS_4

Crystal data	
Chemical formula	Na_3ZnAlS_4
Mr	289.6
Crystal system space group	Tetragonal $I4_1/acd$
Temperature (K)	293
a (Å)	12.9206(1)
c (Å)	18.5822(2)
V (Å^3)	3102.12(4)
Z	16
Data collection	
Radiation type	Cu-Kα
Diffractometer	Rigaku SmartLab
Geometry	Bragg–Brentano
2θ values (°)	$2\theta_{min}$ = 9.94 $2\theta_{max}$ = 120 $2\theta_{step}$ = 0.02
Refinement	
R factors and goodness of fit	R_p = 0.037 R_{wp} = 0.053 R_{exp} = 0.014 $R(F)$ = 0.057 R_B = 0.097 χ^2 = 14.516
No. of parameters	46

Table 3 Anisotropic displacement parameters (Å^2) of Na_3ZnAlS_4

Atom	U_{11}	U_{22}	U_{33}	U_{12}	U_{13}	U_{23}
Na2	0.081(5)	0.075(5)	0.105(5)	−0.006(3)	−0.057(4)	0.012(4)

clusters also shared corners and formed a 3D-$(Zn/Al)_4S_8$ framework (Fig. 3c), within which sodium atoms were located. The interatomic distances and bond valence sums (BVS)[33] of Na_3ZnAlS_4 are listed in Table 4.

In the Zn/AlS_4 tetrahedra, the Zn/Al–S distances varied from 2.281 Å to 2.341 Å with an average $<d_{Zn/Al–S}>$ value of 2.308 Å. This value is lower than the average $<d_{Zn/In–S}>$ value of 2.408 Å observed for Na_3ZnInS_4.[30] This is in good agreement with the increase in the ionic radii of four coordinated aluminum and indium atoms from 0.39 Å to 0.62 Å.[34]

The Na1 and Na2 atoms occupied 32*g* Wyckoff positions, and both atoms were octahedrally coordinated to the sulfur atoms. Furthermore, the $Na1S_6$ octahedra were more regular in shape than the $Na2S_6$ octahedra, even though the average $<d_{Na1–S}>$ and $<d_{Na2–S}>$ distances of 3.003 and 3.035 Å, respectively, were similar (Table 4 and Fig. 3d). These values are similar to the average $<d_{Na–S}>$ of 3.029 and 3.074 Å observed in the Na_3ZnInS_4 compound.[30] In the three Na_3ZnMS_4 compounds (M = Al, Ga, In), the first sodium atom exhibited larger displacement parameters than the second sodium atom (*i.e.*, U_{eq} = 0.0366 Å^2 and U_{eq} = 0.088 Å^2 in Na_3ZnGaS_4 and U_{eq} = 0.0453 Å^2 and U_{eq} = 0.1213 Å^2 in Na_3ZnInS_4). This indicates that the first sodium atom is more mobile than the second one. This was also suggested by Hwang *et al.* in their study on Ca-substituted Na_3ZnGaS_4 compounds.[28] BVS calculations yielded values of 0.90, 1.11, 2.23, and 3.03 for Na1, Na2, Zn1, and Al1, respectively. Only the Zn atom was slightly over bonded. The crystal density of Na_3ZnAlS_4 was calculated to be 2.49 g cm^{-3}.

Fig. S1† shows the SEM-EDS images of Na_3ZnAlS_4 electrolyte. On the EDS mappings, the constituent elements Na, S, Zn and Al were almost uniformly distributed.

To increase the ionic conductivity of Na_3ZnAlS_4, Na vacancies were created by partially replacing Zn with Al. This led to a new composition, $Na_{3-x}Zn_{1-x}Al_{1+x}S_4$ (x = 0.1, 0.15, and 0.2). The XRPD patterns of the compounds are shown in Fig. S2.† All the patterns appear similar, confirming the formation of new phases. Furthermore, when x increased, the diffraction peak 440 at 2θ = 39.5° shifted to higher angles, whereas the peak 004 at 2θ = 19.1° shifted to lower angles. This indicates that the tetragonal cell parameters a and b decrease, while c increases with x. Furthermore, full pattern-matching analyses confirmed these observations. The evolution of the cell parameters as a function of x is shown in Fig. 4 and Table S1.†

For the $Na_{3-x}Zn_{1-x}Al_{1+x}S_4$ (x = 0, 0.1, 0.15, and 0.2) compounds, the lowest and highest ionic conductivities at 25 °C were measured for the compositions x = 0 and 0.1, respectively. Therefore, for clarity, only the temperature dependences of the ionic conductivities of x = 0 and 0.1 are shown in Fig. 5. The Nyquist plot of $Na_{2.9}Zn_{0.9}Al_{1.1}S_4$ (x = 0.1) at 29.8 °C is shown in Fig. S3.† The semicircle in the high-frequency region and spike in the low-frequency region indicate that $Na_{2.9}Zn_{0.9}Al_{1.1}S_4$ is a typical ionic conducting material. Bulk and grain boundary contributions were not separated; thus, the ionic conductivities were calculated from the total resistance R, and this indicates that the $Na_{3-x}Zn_{1-x}Al_{1+x}S_4$ electrolytes possess excellent formability, which enables them to exhibit high ionic conductivity even when pressed at room temperature. The temperature dependence

Table 2 Atomic coordinates and isotropic displacement parameters (Å^2) of Na_3ZnAlS_4

Atom	Wyck.	Occ.	x	y	z	$U_{iso/eq}$
Na1	32*g*	1	0.1143(3)	0.6357(3)	0.87500	0.042(2)
Na2	32*g*	1	0.1333(3)	0.9131(3)	0.9845(2)	0.087(3)
Zn1	32*g*	0.5	0.12142(13)	0.67045(14)	0.06233(12)	0.0168(7)
Al1	32*g*	0.5	0.12142(13)	0.67045(14)	0.06233(12)	0.0168(7)
S1	32*g*	1	0.25000	0.5819(3)	0.00000	0.0240(13)
S2	32*g*	1	0.04505(19)	0.5403(2)	0.12609(18)	0.0244(11)
S3	32*g*	1	0.00000	0.75000	0.98698(18)	0.0139(12)

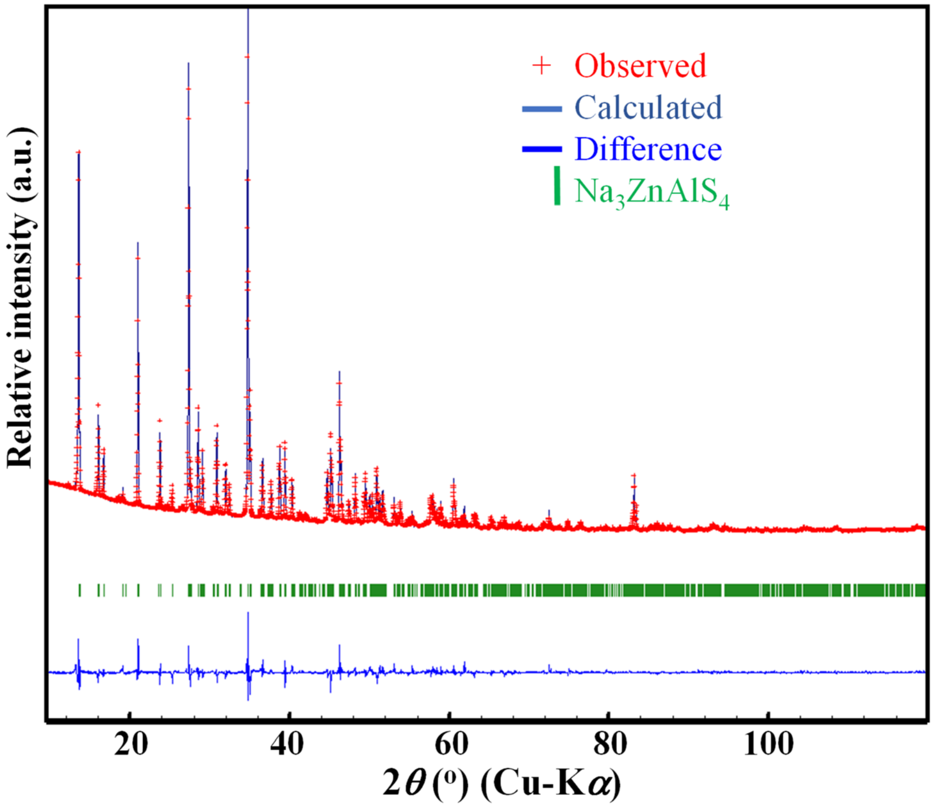

Fig. 2 Observed (cross), calculated (solid line), and difference (bottom) XRPD patterns (Cu-Kα radiation) resulting from Rietveld refinement for Na_3ZnAlS_4. The impurity peaks were excluded.

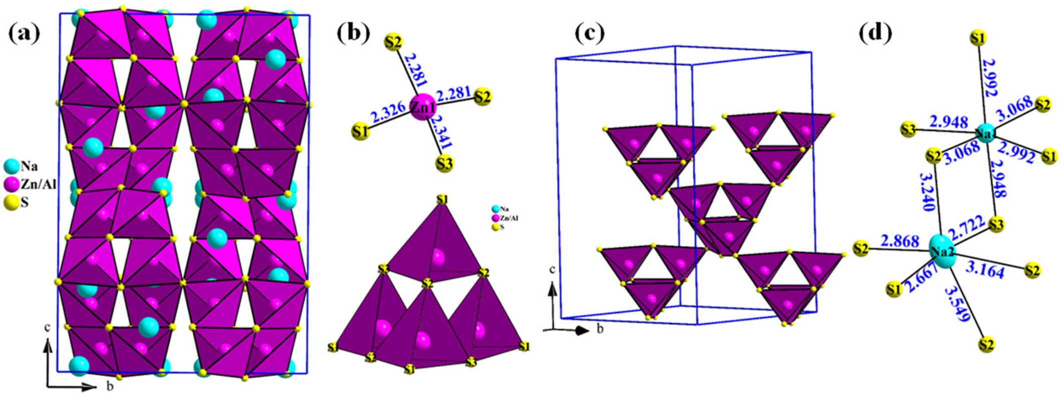

Fig. 3 (a) Projection view of the crystal structure of Na_3ZnAlS_4 along [100], (b) $(Zn/Al)S_4$ tetrahedron and $(Zn/Al)_4S_{10}$ cluster, (c) $(Zn/Al)_4S_8$ framework, and (d) coordination spheres of Na1 and Na2 atoms.

of the ionic conductivities obeyed Arrhenius' law; therefore, the activation energies were obtained from the linear fit of log(σ) *vs.* 1000/T. The ionic conductivities at 25 °C and activation energies are summarized in Table 5.

At 25 °C, the Na_3ZnAlS_4 sample exhibited an ionic conductivity of 3.8×10^{-7} S cm^{-1} (E_a = 37 kJ mol^{-1}), whereas $Na_{2.9}Zn_{0.9}Al_{1.1}S_4$ exhibited an ionic conductivity of 4.5×10^{-6} S cm^{-1} (E_a = 32 kJ mol^{-1}), which is one order of magnitude higher than that of Na_3ZnAlS_4. This was due to the introduction of Na vacancies, which enhanced the ionic conductivity. A similar phenomenon was observed in $Na_{3-x}Zn_{1-x}Ga_{1+x}S_4$-based electrolytes. In a previous study, it was shown that vacancies were introduced at the Na2 sites, which had large ADPs, and the conductivity increased through Na2–Na2 pathways.[27,28]

Fig. 6 and 7 show the XRPD patterns and Raman spectra of $Na_{2.9}Zn_{0.9}Al_{1.1}S_4$ before and after exposure to humid air (relative humidity: 70%) for 30 min. The

Table 4 Interatomic distances (Å) and BVS for Na_3ZnAlS_4

	Distance
Na1–S3 (×2)	2.948(3)
Na1–S1 (×2)	2.992(2)
Na1–S2 (×2)	3.068(5)
	<3.003>*0.90
Na2–S1	2.667(5)
Na2–S3	2.722(4)
Na2–S2	2.868(5)
Na2–S2	3.164(5)
Na2–S2	3.240(5)
Na2–S2	3.550(5)
	<3.035>*1.11
Zn/Al1–S2	2.281(3)
Zn/Al1–S2	2.282(4)
Zn/Al1–S1	2.326(3)
Zn/Al1–S3	2.341(3)
	<2.308>
	*2.23 for Zn
	*3.08 for Al

*Bond valence sum, B. V. = $e^{(r_0-r)/b}$ with the following parameters: b = 0.37, r_0 (Na^I–S) = 2.3 Å, r_0 (Zn^{II}–S) = 2.18 Å, and r_0 (Al^{III}–S) = 2.13 Å. The average distances are expressed as <>.

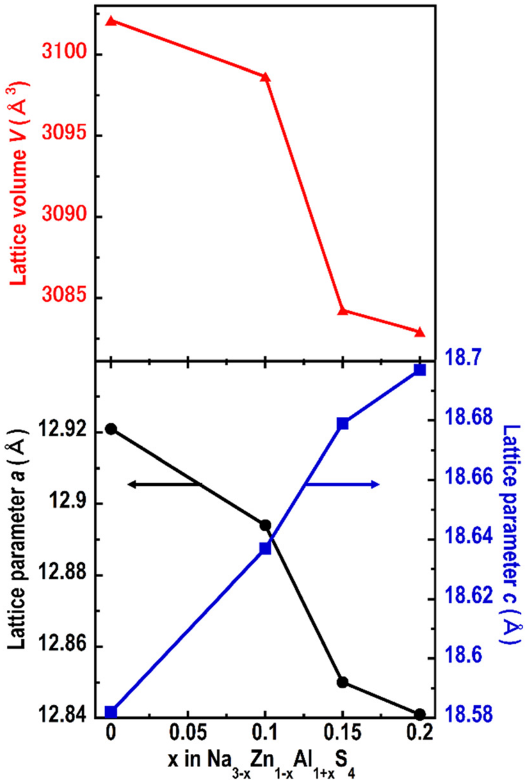

Fig. 4 Evolution of the cell parameters as a function of x in $Na_{3-x}Zn_{1-x}Al_{1+x}S_4$ (x = 0, 0.1, 0.15, and 0.2).

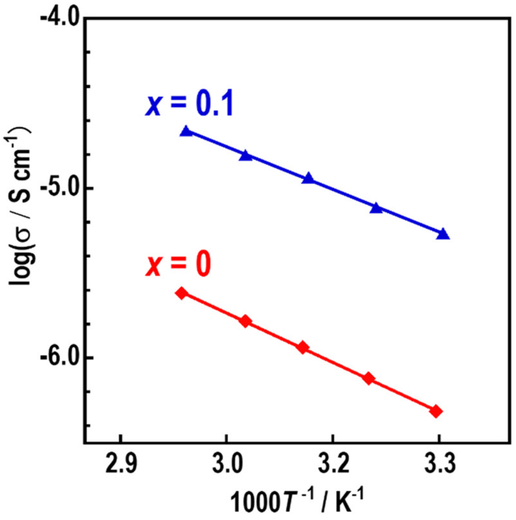

Fig. 5 Temperature dependence of the ionic conductivities (σ) of Na_3ZnAlS_4 (x = 0) and $Na_{2.9}Zn_{0.9}Al_{1.1}S_4$ (x = 0.1).

Table 5 Ionic conductivities at 25 °C (σ_{25}) and activation energies (E_a) of $Na_{3-x}Zn_{1-x}Al_{1+x}S_4$

x	σ_{25} (S cm^{-1})	E_a (kJ mol^{-1})
0	3.8×10^{-7}	37
0.1	4.5×10^{-6}	32
0.15	3.5×10^{-6}	32
0.2	3.8×10^{-6}	36

XRPD pattern of $Na_{2.9}Zn_{0.9}Al_{1.1}S_4$ exposed to humid air was almost identical to that of pristine $Na_{2.9}Zn_{0.9}Al_{1.1}S_4$. However, new impurity peaks, attributable to NaSH, appeared. This was confirmed *via* Raman spectroscopy. On the Raman spectra, the peaks between 100 and 550 cm^{-1}, which were attributed to pristine $Na_{2.9}Zn_{0.9}Al_{1.1}S_4$, did not change after exposure to humid air, even though the peak attributed to S–H (ref. 35) appeared at around 2550 cm^{-1}. The previous study[27,28] indicated that the Na_3ZnGaS_4 compound has a high humidity stability due to its open-channel structure with a network of corner-shared super-tetrahedra. Similarly, the relatively

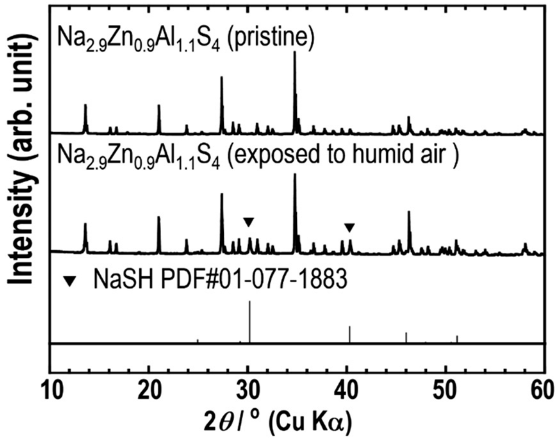

Fig. 6 XRPD patterns of pristine $Na_{2.9}Zn_{0.9}Al_{1.1}S_4$ and $Na_{2.9}Zn_{0.9}Al_{1.1}S_4$ exposed to air.

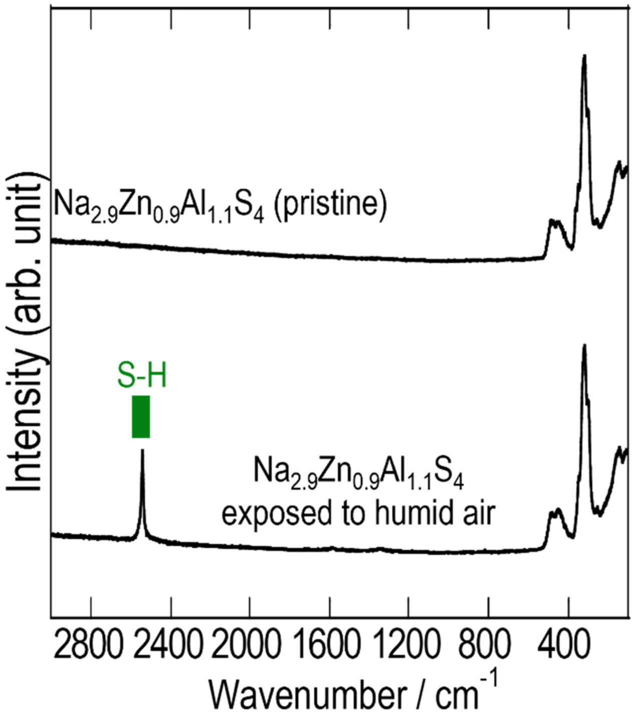

Fig. 7 Raman spectra of pristine $Na_{2.9}Zn_{0.9}Al_{1.1}S_4$ and $Na_{2.9}Zn_{0.9}Al_{1.1}S_4$ exposed to air.

high humidity stability of $Na_{2.9}Zn_{0.9}Al_{1.1}S_4$ when exposed to humid atmosphere for a short time can be correlated with its crystal structure.

Conclusions

The new solid electrolytes ($Na_{3-x}Zn_{1-x}Al_{1+x}S_4$ ($x \le 0.2$)) were prepared for the first time *via* a simple heat treatment using sodium polysulfides. These materials are isostructural with Na_3ZnGaS_4. As the aluminum content increased from 1 to 1.2, the cell volume decreased almost linearly, suggesting the formation of a solid solution. The sodium vacancies introduced by tuning the relative Zn/Al ratio in $Na_{3-x}Zn_{1-x}Al_{1+x}S_4$ enhanced the ionic conductivities, and $Na_{2.9}Zn_{0.9}Al_{1.1}S_4$ exhibited the highest conductivity of 4.5×10^{-6} S cm^{-1} at 25 °C. Moisture stability tests showed that $Na_{2.9}Zn_{0.9}Al_{1.1}S_4$ was relatively stable when exposed to a humid atmosphere.

Data availability

The data supporting this article have been included as part of the ESI.†

Conflicts of interest

There are no conflicts of interest to declare.

Acknowledgements

This work was supported by JSPS KAKENHI Grant Number JP23H02071 and the 2023 Osaka Metropolitan University (OMU) Strategic Research Promotion Project (Priority Research).

References

1 B. L. Ellis and L. F. Nazar, *Curr. Opin. Solid State Mater. Sci.*, 2012, **16**, 168–177.

2 H. Pan, Y.-S. Hu and L. Chen, *Energy Environ. Sci.*, 2013, **6**, 2338.

3 N. Yabuuchi, K. Kubota, M. Dahbi and S. Komaba, *Chem. Rev.*, 2014, **114**, 11636–11682.

4 H.-L. Yang, B.-W. Zhang, K. Konstantinov, Y.-X. Wang, H.-K. Liu and S.-X. Dou, *Adv. Energy Sustainability Res.*, 2021, **2**, 2000057, DOI: **10.1002/aesr.202000057**.

5 A. Hayashi, *Electrochemistry*, 2023, **91**(10), 101002, DOI: **10.5796/electrochemistry.23-00096**.

6 H. Ahmad, K. T. Kubra, A. Butt, U. Nisar, F. J. Iftikhar and G. Ali, *J. Power Sources*, 2023, **581**, 233518.

7 A. Sakuda, A. Hayashi and M. Tatsumisago, *Sci. Rep.*, 2013, **3**, 2261.

8 A. Hayashi, K. Noi, A. Sakuda and M. Tatsumisago, *Nat. Commun.*, 2012, **3**, 856.

9 M. Duchardt, U. Ruschewitz, S. Adams, S. Dehnen and B. Roling, *Angew. Chem.*, 2018, **130**, 1365–1369.

10 Z. Zhang, E. Ramos, F. Lalère, A. Assoud, K. Kaup, P. Hartman and L. F. Nazar, *Energy Environ. Sci.*, 2018, **11**, 87–93.

11 F. Tsuji, K. L. Hoh, K. H. Kim, A. Sakuda, M. Tatsumisago, S. W. Martin and A. Hayashi, *J. Ceram. Soc. Jpn.*, 2021, **129**, 323–328.

12 A. Banerjee, K. H. Park, J. W. Heo, Y. J. Nam, C. K. Moon, S. M. Oh, S. T. Hong and Y. S. Jung, *Angew. Chem.*, 2016, **128**, 9786–9790.

13 H. Wang, Y. Chen, Z. D. Hood, G. Sahu, A. S. Pandian, J. K. Keum, K. An and C. Liang, *Angew. Chem.*, 2016, **128**, 8693–8697.

14 L. Zhang, D. Zhang, K. Yang, X. Yan, L. Wang, J. Mi, B. Xu and Y. Li, *Adv. Sci.*, 2016, **3**, 1600089, DOI: **10.1002/advs.201600089**.

15 F. Tsuji, S. Yubuchi, A. Sakuda, M. Tatsumisago and A. Hayashi, *J. Ceram. Soc. Jpn.*, 2020, **128**, 641–647.

16 F. Tsuji, N. Masuzawa, A. Sakuda, M. Tatsumisago and A. Hayashi, *ACS Appl. Energy Mater.*, 2020, **3**, 11706–11712.

17 A. Nasu, T. Otono, T. Takayanagi, M. Deguchi, A. Sakuda, M. Tatsumisago and A. Hayashi, *Energy Storage Mater.*, 2024, **67**, 103307.

18 T. A. Yersak, Y. Zhang, F. Hao and M. Cai, *Front. Energy Res.*, 2022, **10**, 882508, DOI: **10.3389/fenrg.2022.882508**.

19 A. Fukushima, A. Hayashi, H. Yamamura and M. Tatsumisago, *Solid State Ionics*, 2017, **304**, 85–89.

20 G. Sahu, Z. Lin, J. Li, Z. Liu, N. Dudney and C. Liang, *Energy Environ. Sci.*, 2014, **7**, 1053–1058.

21 T. Kimura, A. Kato, C. Hotehama, A. Sakuda, A. Hayashi and M. Tatsumisago, *Solid State Ionics*, 2019, **333**, 45–49.

22 K. Kanazawa, S. Yubuchi, C. Hotehama, M. Otoyama, S. Shimono, H. Ishibashi, Y. Kubota, A. Sakuda, A. Hayashi and M. Tatsumisago, *Inorg. Chem.*, 2018, **57**, 9925–9930.

23 H. Tang, Z. Deng, Z. Lin, Z. Wang, I.-H. Chu, C. Chen, Z. Zhu, C. Zheng and S. P. Ong, *Chem. Mater.*, 2018, **30**, 163–173.

24 T. Takayanagi, A. Nasu, F. Tsuji, K. Motohashi, A. Sakuda, M. Tatsumisago and A. Hayashi, *J. Ceram. Soc. Jpn.*, 2022, **130**, 22017.

25 H. Gamo, N. H. H. Phuc, H. Muto and A. Matsuda, *ACS Appl. Energy Mater.*, 2021, **4**, 6125–6134.

26 S. Balijapelly, Q. Zhang, P. Sandineni, A. Adhikary, S. Mohapatra, S. Sundaramoorthy, N. Gerasimchuck, A. V. Chernatynskiy and A. Choudhury, *ACS Appl. Energy Mater.*, 2021, **4**, 7942–7951.

27 S. Han, J. Y. Seo, W. B. Park, A. B. Ikhe, S. Y. Choi, S. C. Han, K.-S. Sohn and M. Pyo, *J. Mater. Chem. A*, 2022, **10**, 25039–25046.

28 E. H. Hwang, J. Y. Seo, W. B. Park, S. Y. Kang, K.-S. Sohn and M. Pyo, *J. Power Sources*, 2023, **581**, 233511.

29 J. Y. Seo, W.-B. Park, S. Y. Kang, Y.-K. Lee, K.-S. Sohn and M. Pyo, *Energy Storage Mater.*, 2024, **65**, 103123.

30 R. Chen, X. Wu and Z. Su, *Dalton Trans.*, 2018, **47**, 15538–15544.

31 V. Petříček, M. Dušek and L. Palatinus, *Z. Kristallogr. - Cryst. Mater.*, 2014, **229**, 345–352.

32 S. J. Clarke and F. J. Disalvo, *J. Alloys Compd.*, 1998, **274**, 118–121.

33 I. D. Brown and D. Altermatt, *Acta Crystallogr., Sect. B: Struct. Sci.*, 1985, **41**, 244–247.

34 R. D. Shannon, *Acta Crystallogr., Sect. A: Cryst. Phys., Diffr., Theor. Gen. Crystallogr.*, 1976, **32**, 751–767.

35 P. Bazylewski, R. Divigalpitiya and G. Fanchini, *RSC Adv.*, 2017, **7**, 2964–2970.